WILEY-VCH

The bright X-ray stimulated luminescence of HfO2 nanocrystals activated by Ti ions.

*Iren Villa Feder ico Moretti, Mauro Fasoli, Antonella Rossi, Bodo Hattendorf, Christophe Dujardin, Markus Niederberger, Anna Vedda, and Alessandro Lauria**

Dr. I. Villa, Prof. M. Fasoli, Prof. A. Vedda
Department of Materials Science, University of Milano-Bicocca,
Via R. Cozzi, 55, 20125 Milano, Italy

Prof. A. Rossi
Dipartimento di Scienze Chimiche e Geologiche, Università di Cagliari,
S.S. 554 Bivio per Sestu, 09042 Monserrato, Cagliari, Italy and ETH Zürich, Department of Materials,
Vladimir-Prelog-Weg 5, 8093 Zürich, Switzerland

Dr. F. Moretti±, Prof. C. Dujardin
Institut Lumière Matière UMR5306 CNRS Université Claude Bernard Lyon 1,
Bâtiment Kastler, 10 rue Ada Byron, 69622 Villeurbanne CEDEX, France.
±(now at Lawrence Berkeley National Laboratory, 1 Cyclotron road, Berkeley, CA 94720, USA)

Dr. B. Hattendorf
Laboratory of Inorganic Chemistry, Trace Element and Microanalysis, ETH Zürich,
Vladimir-Prelog-Weg 1, 8093 Zürich, Switzerland
Prof. Markus Niederberger, Dr. Alessandro Lauria
Laboratory for Multifunctional Materials, ETH Zürich,
Vladimir-Prelog-Weg 5, 8093 Zürich, Switzerland
E-mail: alessandro.lauria@mat.ethz.ch

Keywords: scintillation, titanium, radioluminescence efficiency, hafnium oxide nanoparticles, decay time.

The recent trends in scintillator technologies stimulate research efforts towards the development of novel materials morphologies such as nanoparticles, able to efficiently convert ionizing radiations into light. For example, scintillating nanoparticles attract great interest in medical oncological therapies. In this work, the structural and morphological properties of HfO2:Ti nanoparticles with Ti concentrations from 0.03 to 10 mol% and subjected to calcination up to 1000 °C are thoroughly characterized; moreover, X-ray photoelectron spectroscopy reveals the incorporation of Ti in both Ti (III) and Ti (IV) chemical states in as prepared samples, while the exclusive presence of Ti(IV) is unambiguously identified in calcined nanoparticles.
The optical emission under X-ray excitation evidences an intense Ti (IV)-related luminescence at 2.5 eV in high temperature calcined samples with a few microseconds scintillation lifetime, and efficiency comparable to that of Bi4Ge3O12 reference scintillator. Finally, the competitive role of defects in charge carriers capture is demonstrated by the monotonic increase of the 2.5 eV band during prolonged X-ray irradiation, more evident for nanoparticles with titanium concentration below 1 mol%. HfO2:Ti might also find application in X-ray triggered oncological therapies by using the Ti (IV)-related bright radioluminescence to excite photosensitizer molecules for singlet oxygen generation.

1. Introduction

Luminescent inorganic nanoparticles (NPs) of various compositions are attracting a vivid interest by virtue of their phase homogeneity, enhanced tunability of the physical and chemical properties, and suitability for the design and fabrication of nanocomposites.[1] In recent years, modern synthesis routes have led to the fabrication of new nanoscale materials with outstanding optical properties arising from their improved crystal phase and composition, narrow size distribution, and uniform shape.[2, 3] Luminescent NPs – metals, semiconductors, or insulators - have come to the forefront in modern solid state physics, lighting, next generation electronics and sensing, in the environmental and life science, as well as in medical and biological fields.[4-13] In particular, extensive theoretical and spectroscopic studies of the optical response of inorganic luminescent NPs have been proving the suitability of these systems in the field of phosphors and scintillators for lighting and radiation detection applications.[9, 14-18] For instance, defect-engineering strategies can be applied in wide band gap nanomaterials. The tuning of their intrinsic luminescence properties, which are mostly due to optically active intrinsic defects
and self-trapped excitons,[19-22] results from chemical and structural modifications, surface restructuring, and lattice reconfiguration (i.e, crystal growth, sintering, and rearrangement of lattice defects).[19, 23] In turn, other studies have revealed the possibility to modify the materials emission colour through doping routes. A well-known way of increasing the luminescence performance of nanoparticles is based on extrinsic centres consisting of the incorporation of rare earth (RE) or transition metal (TM) ions in the crystal lattice.[24-31]

Regardless of the emission type – either intrinsic or extrinsic – the design of novel scintillating nanoparticles is mostly focused on optimizing their ability to efficiently convert the absorbed ionizing energy into visible (Vis) or near ultraviolet (UV) light.[32] In this framework, the research of new strategies for defect engineering and doping is active, coupled to the unceasing investigation directed to the comprehension of the physical phenomena occurring between the host lattice and optically active centres.[33]

Hafnium dioxide (hafnia - HfO_2) is considered a versatile nano-system by the materials science community.[34] Indeed, the more recent advances in colloidal preparation techniques have allowed the production of HfO_2 crystalline nanoparticles with diameter below 5 nm, overcoming the difficulty of bulk growth (due to its very high melting point of over 2700 °C).[35] Hafnia presents specific features, such as high density (9.7 g/cm3) and high atomic number of Hf (Z= 72) ensuring high absorption efficiency of the ionizing radiation, and a band gap of ~ 5.6 eV, which, in turn, makes this material a suitable host for luminescent dopant ions.[15, 26, 36-44] In addition to the extrinsic luminescence, related to the dopant, previous studies found a broad emission band specific for the undoped monoclinic HfO_2 lattice under either UV or X-ray irradiation. The presence of a fast blue photoluminescence (PL) and radioluminescence (RL) band has been evidenced. This emission is characterized by a decay time in the ns range and results from oxygen vacancy - related defects. At the same time, the occurrence of a quite efficient blue luminescence has been observed, with a lifetime of a few μs and an extrinsic origin due to titanium incidental impurities in the nano-hafnia lattice.[19, 45-47] In the literature, the effect of the introduction of small amounts of transition metal in metal oxides nanomaterials and thin films, such as HfO_2 and ZrO_2 has been considered in order to change their dielectric properties.[48-53] Nevertheless, just a few works in the literature covered the PL and RL features of Ti - doped metal oxides. For instance, Ti - doped Zr oxide materials have been recently proposed as RE- free blue phosphors for industrial applications, stress indicators, damage sensors, and other mechano-optical devices, which take advantage of the bright mechanoluminescence of these systems.[29, 54, 55] Lanthanum hafnates single crystals have attracted considerable interest as scintillators thanks to the enhancement of their luminescence properties due to Ti incorporation.[56]

Fiaczyk et al. explored the luminescent properties of HfO2:Ti sintered ceramics as a function of temperature.[57, 58] Despite the increasing interest, the luminescence features of Ti ion have not yet been fully characterized and their investigation still deserves attention, especially under ionizing radiation and in nanometric materials. Indeed, the blue Ti-related luminescence can be suitable to excite oxygen photosensitizer molecules, like porphyrins, opening application perspectives of this high-density nanomaterial in the field of medical therapy.[59]

In this work, a systematic study of the structural and optical features of monoclinic Ti-doped hafnia nanocrystals under X-ray irradiation was performed to elucidate the dependence of RL emission on the calcination conditions, crystal growth, defectiveness of the NPs, as well as on the dopant concentration. The comprehension of the luminescence mechanisms is mandatory to pave the way for developing new highly efficient hafnia at the nanoscale for future applications as scintillators.

2. Material composition, morphology, and structure

HfO2 NPs were obtained by non-aqueous sol–gel synthesis and they were doped by the addition of dopant precursors to the reaction mixture.[26, 37, 60] The morphology, structure and composition of all Ti-doped nanopowders was explored through transmission electron microscopy (TEM) (Figure 1 a - e), laser ablation inductively coupled plasma mass spectrometry (LA-ICPMS) (Figure 1 g),[61] and X-ray powder diffraction (XRD) (Figure 1 f and h).

After the reaction between Hf t-butoxide and Ti (III) chloride in benzyl alcohol, crystalline monoclinic NPs were obtained for different doping levels (Figure 1 a-c, f) and calcination treatment (Figure 1 d, e, h). The elemental analysis in Figure 1 g of pressed powder samples, confirms a good agreement of the experimentally measured concentrations of Ti with the nominal ones; the slightly higher values of the experimental data with respect to the nominal ones might be ascribed to an additional content of Ti ions deriving from unintentional impurities (upto hundreds of ppm) in the Hf precursor itself, as already reported for similar materials.[19] No additional segregated phases such as titanium oxide are visible, regardless of the Ti nominal content, even after calcination, confirming that Ti ions are incorporated in the HfO2 lattice in all samples (Figure S1). The HfO2 crystals average size, calculated by the Scherrer formula on the diffractogram, lies in the 3-8 nm range and is weakly dependent on the dopant concentration both in the as-synthesized as well as in the Ti doped NPs calcined at 500 °C (Figure 1 i, blue circles and green triangles, respectively). At this temperature the decomposition of the organic ligand shell bound to the NPs surface is usually observed.[19] Figure 1 d and e show representative TEM images of 0.3 mol% Ti doped HfO2 powders after calcination at 500 and 1000 °C, respectively. The observed clustering of the NPs (Figure 1 d), starting at a temperature of 500 °C, is due to severe reconfiguration of the material at the nanoscale. The degradation of the organic ligands on the surface certainly contributes to the agglomeration of the NPs.[19, 26]

In turn, the role of concentration of the Ti ions and of the temperature in altering the coalescence and crystal reconfiguration of the NPs is mostly evident when considering the calcination at 1000 °C. As expected, TEM images (Figure 1 e) and XRD data (Figure 1 h and i)) evidence a crystal growth and coalescence of originally separated nanocrystals as a function of increasing temperature, in accordance with the role of the additional heat provided. However, clearly lower average crystal sizes are observed for doping higher than 1 mol% (Figure 1 i, pink squares). This complex picture suggests that, differently than for low doping levels, higher Ti loading may hinder the hafnia lattice re-crystallization process, leading to smaller crystalline domains in the calcined nanopowders, resulting from the less pronounced crystal growth. A similar behaviour has been already reported in Hf-based thin films after the introduction of Zr or Ti dopant ions, having smaller grain sizes at higher doping levels.[62, 63]

The structural and spectroscopic results on Ti doped hafnia NPs are consistent with some previously reported experiments and theories regarding the change in structure (from monoclinic to cubic phase)

of HfO2 and its isomorph ZrO2. Indeed, the crystal phase transition from their monoclinic to the cubic arrangement can be achieved at low temperature by doping. In the literature, the origin of the stabilization of high-temperature cubic phase in HfO2 is related to both the dopant ion size and to the oxygen vacancies concentration, depending on the valence of the dopant substituting for Hf in the lattice.[64] For instance, the stabilization of the cubic phase in these systems can be achieved through the incorporation of trivalent or divalent ions into the lattice, and the subsequent generation of oxygen vacancies for charge compensation.[26, 40, 47, 65, 66, 67, 68] Other papers, based on the density functional theory, have imputed the HfO2 transition from the monoclinic to the cubic phase to the incorporation of dopants (for instance Y, Eu, and Gd) with ionic radii larger than that of the Hf ion (0.76– 0.83 Å) and thus to an increase of the strain of the lattice.[39, 69] The lack of structural change evidenced in hafnia NPs after doping with Ti (Figure 1 f and h) can be mainly due either to its ionic radius, which is significantly smaller than that of Hf and not able to stabilize the cubic phase at the considered concentrations, or to its valence. In fact, tetravalent titanium can be included in HfO2 matrix by substituting Hf4+ ions. In this case, the replacement of isovalent cations, not requiring charge compensating oxygen vacancies, could be a reason preventing the stabilization of the cubic crystal structure even at high Ti doping levels.[70] XPS analysis was applied to monitor the Ti chemical state in doped hafnia NPs before and after calcination at 1000 °C (Figure 2). The titanium spectrum of the 1% doped Ti:HfO2 NPs before calcination exhibits two components: one at 459.2 eV and another less intense one at 457.00 eV, assigned to Ti (IV) and Ti (III) in their corresponding oxides. These values are in agreement with those reported in the literature.[71, 72] It is worth noting that the peak at lower binding energy might be influenced by the presence of the Hf4p signal that is usually revealed at 454.3 eV. After heat treatment at 1000 °C, the spectrum still exhibits the main component at 459.2 eV while the one at lower binding energy is shifted to 458.6 eV, indicating the oxidation of the Ti (III) to Ti (IV), as expected during calcination in air. The results suggest the incorporation of Ti ions in the HfO2 nanocrystal lattice mainly in the form of Ti (IV), with a minor amount of Ti (III), which gets oxidized during the calcination process. Indeed, also the signals of O1s and Hf4f, recorded on the same samples, reveal a change of the peak position and of the width of these signals (Figure S5 in supporting information) induced after calcination. These experimental findings, in agreement with XRD and TEM results, can be interpreted as due to a crystal reconfiguration, which leads to the lowering of distorted lattice sites in calcined samples.

3. Radioluminescence

The spectrally corrected RL of the most representative Ti concentrations, recorded at room temperature (RT), are reported in Figure 3. The RL emission, studied by increasing the concentration of titanium from 0.3 mol% up to 10 mol% (Figure 3 a - d) in untreated samples and after calcination at 500 °C and 1000 °C, evidences the role of Ti nominal amount as well as of the thermal treatments in the evolution of the luminescence features. The spectra of additional samples are reported in Figure S2. The untreated powders display a broad complex emission ranging from 1.5 to 4.0 eV. The RL emission of undoped HfO2 NPs was previously demonstrated to be composed of up to 4 bands in the Vis- near UV range,[47] and the addition of Ti dopant operated in this work leads similar RL features before thermal treatments (Figure 3, blue curves). RL spectra of untreated powders indeed reveal a multicomponent emission in the blue region, apparently peaked at 2.25 eV, together with a second near-UV emission centred at 3.4 eV. The intensity ratio between the Vis/UV emission bands increases with the nominal amount of titanium (Figure S6). Precisely, at Ti concentrations lower than 0.3 mol%, the near-UV band is more intense than the blue one (Figure S2a), while it decreases to zero for higher concentrations (Fig 3, blue curves). When hafnia is treated at 500 °C, the RL spectrum is composed only of the visible band shifting from higher to lower energies while the dopant content increases. At Ti concentrations

up to 1 mol%, the maximum of the RL spectrum is at 2.50 eV; in turn, it shifts apparently to 2.25 eV for titanium concentrations of 3 and 10 % mol, similarly to the untreated NPs. After calcination at 1000 °C, the most intense band turns out to be the one peaking at 2.50 eV, which clearly dominates the spectrum for all titanium concentrations.

These observations well agree with previous results, where the broad luminescence of undoped HfO2 NPs, treated at low temperature, has revealed an intrinsic origin both under near UV excitation and ionizing radiation.[19, 47] Spectroscopic investigations and computational calculations by density functional theory (DFT) have evidenced that oxygen vacancies play a major role as defect centres responsible for the optical emissions in hafnia. In fact, different variants of oxygen vacancies have been related to additional electronic levels within the band gap of HfO2.[45, 73-84]Nevertheless, in nominally pure HfO2 NPs, the intrinsic defect-related band centred at around 2.50 eV overlaps with the blue emission due to accidental Ti impurities in the matrix. The two PL emissions at 2.50 eV are distinguishable by both their different excitation profiles and by their very different time decays. Indeed, the intrinsic one is excited by near-UV wavelengths about 340 nm and it decays in the ns time range, while the Ti-related luminescence becomes predominant under 250 nm excitation, only after calcination of the NPs at high temperature, and it features a PL time decay in the μs range.[19] By considering this background, RL measurements on Ti-doped HfO2 seem to display a clearer picture about the role of Ti and thermal evolution of the nanomaterials. Before calcination, the Ti-related luminescence is silent despite its presence in the lattice. The RL of untreated powders is rather intrinsic and caused by defect centers. This well agree with XPS evidences, pointing at the occurrence of both Ti (IV) and Ti (III) at the very initial stage of the structural evolution operated by the annealing (Figure 2). Since the presence of trivalent dopant ions involves charge compensation in HfO2, Ti(III) ions can influence the intrinsic defectiveness of the nanoparticles, resulting in changes in the relative intensity of the luminescence in the visible and UV range, that are still not fully understood. At the intermediate calcination temperature of 500 °C, the nanoparticles preserve the small diameter close to the ones of untreated Ti:HfO2 (Figure 1i), suggesting a still important presence of intrinsic emissions due to defects, similar to what previously observed in undoped HfO2. [19] The NPs nevertheless undergo agglomeration, while optically active defects, such as oxygen vacancies and organic residuals on the surface of the NPs, start being altered or degraded by oxidation phenomena. The complex RL profiles result from the concomitant luminescence of intrinsic defects and Ti centers, which are only partially active at this stage. Indeed, this Ti-related component at higher energy, seems to be quenched for Ti concentration higher than 1%. As a consequence, the multicomponent RL of semi-treated powders mildly doped (0.3 and 1 % Ti), increases and is centred at higher energies (Figure 3, green curves and Figure 4, green circles). When instead the Ti emission is quenched (3 and 10 % Ti) the RL profile remains unchanged, as also its intensity does (Figure 4 and Figure 3 c,d).

After annealing further up to 1000 °C, Ti-related RL at 2.5 eV becomes dominant, at all concentrations, and the apparent blue shift of the RL profiles reaches completion. The size of the nanocrystals and their crystalline degree increase with the temperature. This severe structural reconfiguration lowers the occurrence of defects and surface states, and the corresponding set of emissions (from 1.5 eV to 4.5 eV), observed in untreated materials, disappear. At the same time, the charge carriers, created during X-ray irradiation of the nanoparticles, can migrate across the material and reach the Ti centers more efficiently. All these factors are responsible for the increase of its blue emission at 2.5 eV, for the highest thermal treatment, by 3 orders of magnitude (Figure 4), which substantially explains the whole RL of Ti:HfO2, for all Ti concentrations. This emission belongs to the charge transfer transition of Ti (IV), whose presence is unambiguously demonstrated by XPS data.[58] The internal quantum yield (iQY) of this transition, measured in 0.3 mol% HfO2:Ti calcined at 1000 °C by exciting at 280 nm, shows a value around 33 %, while the external quantum efficiency (EQE) is of about 24.0 % (see

"Experimental" for definition of efficiency and measurement details). In Figure S3 the time resolved photoluminescence (TR-PL) decays of HfO2 NPs calcined at 500 °C and 1000 °C are also reported. In NPs calcined at 1000 °C (Figure S3 a), the TR-PL profile of the intense 2.50 eV peak under UV irradiation shows a double exponential decay with an overall half-life of 4 □s, confirming the presence of optically active Ti centres responsible for the blue emission. In turn, hafnia NPs treated at 500 °C display the occurrence of the fast intrinsic luminescence (<t> = 5 ns) under excitation at 340 nm (Figure S3b and d), together with the existence of a slower component likely due to Ti ions when irradiating at 250 nm (Figure S3a). The slight discrepancy from the value found for NPs calcined at 1000 °C can be due to the different structural and dimensional properties of the two samples induced by different calcination temperatures. Figure 4 shows the RL efficiency, expressed as the integral of the RL composite band from 1.50 eV to 4.0 eV, as a function of the Ti concentrations.

Bi4Ge3O12 (BGO) powder efficiency is shown as standard reference value. The sample reveals no significant variations up to titanium concentration of 3 mol% before the calcination process. In turn, all the calcined hafnia nanocrystals present a general increase of the emission intensities with increasing the dopant concentration. When Ti concentration reaches the value of 1 mol%, a decrease of light output occurs, possibly due to concentration quenching. In particular, for Ti doping content between 0.1 and 1 mol% in hafnia nanocrystals calcined at 1000 °C, the RL output is even higher than that of the BGO reference. In general, the results may underline the different origins of hafnia RL bands. The intrinsic ones in the untreated samples have just a weak dependence on Ti amount. Conversely, the RL intensity of the 2.5 eV dominant band in calcined NPs is related to the presence of titanium as optical centre and displays a different behaviour upon both the doping level and the calcination temperature. Actually, the calcination is known to induce changes in the morphological characteristic parameters, such as the increase of the NPs size, as shown in Figure 1, as well as the reduction of defects-related trapping centres. These structural and defectiveness modifications promote a more efficient carriers transport to the titanium centres during the RL process, thus leading to a higher luminescence signal.

4. RL hysteresis

A sequence of RL measurements under continuous irradiation has been conducted in order to provide a deeper insight on the emissions stability, which is a crucial feature for application performances. **Figure 5** shows a complete analysis of the stability response of Ti doped hafnia nanocrystals under X-ray irradiation during a time range of hundreds of seconds. A total cumulated dose of approximately 50 Gy, evaluated on quartz powder as reference material, was imparted to the samples using a dose rate of 9.97 mGy/(ms*mA). The displayed results (Figure 5a,b) show that the emission stability of untreated samples is only slightly affected by the irradiation time. The NPs calcined at 500 °C display a dual behaviour: no meaningful variations are evident for Ti concentrations higher than 3 mol%, while for lower concentrations a slight RL increase is detected. Results in Figure 5c clearly evidence the role of Ti concentration in affecting the RL intensity versus irradiation time in larger nanocrystals treated at 1000°C. The recorded measurements show a continuous RL increase which exceeds, in the first 3 minutes of irradiation, the initial intensity value by more than 10%. This effect is less pronounced as the Ti concentration is increased. On the contrary, at the maximum doping concentration the RL signal is even decreasing. The enhancement of the RL yield observed after a large amount of radiation exposure is called *hysteresis or brightburn or memory effect*.[87-89] The scintillation process requires the conversion of ionizing radiation into a multitude of free electrons and holes, their transfer to the luminescent centres, and the final radiative recombination of the excited centres to emit photons

in the visible or ultraviolet range. The transfer stage, in particular, involves the migration of the free carriers, thus being susceptible to the presence of lattice imperfections acting as traps. In our experiment, the RL of untreated hafnia NPs is weakly affected by the presence of competitive traps, maybe due to the intrinsic nature of the luminescence. On the contrary, in calcined samples the progressive trap filling, due to continuous irradiation, increases the probability for free carriers to end on a recombination centre, here represented by titanium, and causes the observed RL sensitization. The competition between carrier trapping and radiative recombination on luminescent centres in hafnia is strongly dependent on the concentration of Ti centres, as seen in Figure 5c. Actually, for high concentration of dopant, the competitive role of defects acting as traps is reduced and the hysteresis effect is no longer observed.

5. Scintillation

One crucial feature in scintillator application is the time response of the phosphor upon irradiation with ionizing radiation. Scintillation decays in the hundreds of ns range or shorter are typically considered necessary for real-time dosimetry, PET imaging detectors, and high- energy physics. Longer times occurring between the ionizing radiation absorption and radiative

recombination are, instead, suitable for X-ray screens for several diagnosis and therapy treatments, where a timely emission is not mandatory.[90]

The scintillation kinetics of titanium in the HfO2 NPs is reported in Figure 6. The scintillation decay was obtained on 1 mol% Ti-doped NPs calcined at 500 °C and 1000 °C , where the maximum RL light output at 2.5 eV is evident (see Figure 4). After background removal, scintillation time decay data of Ti doped NPs calcined at 1000°C can be fitted by a double exponential function. In accordance with the TR-PL picture described above, the NPs calcined at high temperature show a lifetime of $\langle\tau\rangle = 6$ □s, characteristic of Ti emission. The decay signal of hafnia calcined at 500 °C is analysed by a multi-exponential fit, composed by a very fast component of almost 1.6 ns, a second component of few tens of ns, and a slowest third component in the time range of hundreds of ns. The presence of the fast component is in good agreement with a previous investigation on undoped hafnia NPs.[47] The monitored band at 2.5 eV has shown a lifetime in the order of a few ns and has been related to intrinsic matrix defects, likely oxygen vacancies. In turn, the slower component can be imputed to titanium centres. The mismatch with respect to the even longer scintillation decay in NPs calcined at higher temperature can be imputed to different morphological and defectiveness properties of the two samples.

6. Conclusion

In this work HfO2 monoclinic nanoparticles have been synthesized and doped with titanium. No additional Ti-related crystal phases have been found for concentrations up to 10 mol%, suggesting its complete incorporation in the host lattice. The emission properties of titanium doped hafnia have been investigated by radioluminescence measurements, revealing an active role of calcination in increasing the intensity of the 2.5 eV Ti-related band that dominates the emission spectrum after calcination at 1000 °C. The XPS analysis of the chemical state of Ti in our materials hints at the occurrence of both Ti(IV) and Ti(III) sites in the as-prepared nanocrystals. High temperature calcination leads to the oxidation of Ti(III) concomitant to the rearrangement of the lattice in a less defective matrix, both phenomena clearly beneficial for the improvement of RL efficiency.

This study has evidenced the high potential of Ti-doping ions as activators of high efficiency radioluminescence in HfO2 nanocrystals. The possibility of controlling the Ti-related luminescence output through the choice of the dopant concentrations, as well as of the calcination temperatures, provides a tool to obtain a reduction of non-radiative channels and an efficient charge transport to the optically active Ti centers, thus resulting in the improvement of the luminescence efficiency under X-ray irradiation. Indeed, the light output of HfO2 nanoparticles doped in the 0.3 -1 mol% range and calcined at 1000 °C is even higher than that of a reference BGO scintillator. Future applications of Ti doped hafnia nanoparticles as nanoscintillators can be foreseen and will be pursued especially in medical fields.

7. Experimental Section

Synthesis of HfO_2 nanocrystals

Hafnium(IV) tert-butoxide (99.99%+Zr), were purchased from Strem Chemicals. Titanium (III) chloride (TiCl3) anhydrous, and benzyl alcohol anhydrous (99.8%) have been purchased from Sigma-Aldrich. All precursors were used without further purification.
Syntheses by solvothermal sol-gel were carried out in a glovebox (O2 and H2O < 0.1 ppm). In a typical synthesis, hafnium(IV) t-butoxide was added to anhydrous benzyl alcohol (BnOH) into a glass test tube. Ti doping at concentrations ranging from 0.03 up to 10 mol% with respect to Hf were achieved by adding appropriate amounts of TiCl3 to the solvent, before addition of the Hf precursor. A total amount of 2.4 mmol of precursors, and a total volume of 20 mL mixtures was used. The mixture was placed into a teflon liner of 45 mL, slid into a steel autoclave (acid digestion vessel mod. 4744 by Parr Instrument Company, USA) and sealed tightly. The autoclave was taken out of the glovebox and heated in a furnace (Memmert, Germany) at 220 °C for 96 hours. The synthesis resulted on a milky suspension that has been centrifuged; the precipitate was washed with diethyl ether (Aldrich), and successively dried in air at 60 °C overnight. Calcined samples were obtained by placing powders in quartz crucibles, heated in a muffle oven (Nabertherm) at both 500 °C and 1000 °C in air, with a heating rate of 10 °C/min and a stasis at the final temperature of 2 hours.

Characterization

Transmission electron micrographs (TEM) were recorded on a Philips FEI Tecnai F30 microscope operated at 300 kV on samples prepared by depositing 10 □l of washed NPs dispersed in absolute ethanol (Aldrich) onto carbon coated Cu grids.X-ray diffraction (PXRD) measurements were performed in reflection mode (Cu Ka radiation at 45 kV and 40 mA) on a Empyrean diffractometer from PANalytical (Netherlands). The RL measurements were carried out at room temperature (RT) using a home-made apparatus featuring, as detection system, a charge coupled device (CCD) (Jobin-Yvon Spectrum One 3000) coupled to a spectrograph operating in the 200-1100 nm range (Jobin-Yvon Triax 180). All spectra were recorded through a 100 line/mm grating. RL excitation was obtained by X- rays irradiation through a Be window, using a Philips 2274 X-ray tube with tungsten target operated at 20 kV. The data were corrected for the spectral response of the detection system. A reference sample of Czochralski bismuth germanate (BGO) crystal, successively grinded into a fine micro-powder, was used for the estimation of the RL efficiency. Pulsed X-ray decay measurements were obtained with a time correlated single photon counting (TCSPC) system composed by a fast photomultipler (SMA650) and TCSPC

electronics (PicoHarp 300) both from PicoQuant. The excitation was performed with a Hamamatsu N5084 light-excited X-ray tube set at 30 kV as irradiation source. The optical excitation of the tube was done with a Hamamatsu PLP-10 picosecond light pulser. The emission wavelength was selected by using a Thorlabs FL400 long-pass interferential filter to eliminate possible interferences with the excitation laser. XPS measurements were performed on powdered samples deposited and pressed in small cuvettes in ambient conditions using a PHI Quantera^{SXM} (ULVAC-PHI, Chanhassen, MN, U.S.A.) spectrometer equipped with a focused and scanned monochromatic Al Kα X-ray source with beam diameter of 100 μm at 25 watt. The emitted electrons were collected at an emission angle, θ, of 45 degrees. The emission angle is defined as the angle between the normal to the sample surface and the axis of the lens. The spectrometer is also equipped with a high- performance floating-column ion gun and an electron neutralizer, used for charge compensation during the analysis on semiconductor/insulator materials. XPS spectra were acquired in fixed analyser transmission (FAT) mode, the pass energy being set to 69 eV and the step size to 0.125 eV. The full width at half maximum (fwhm) of the Ag $3d_{5/2}$ peak height is 0.86 eV in this analysis conditions; in the case of the sample with only 1% Ti doping the pass energy was set at 112 eV for the acquisition of the narrow scans (step-size 0.1 eV). Survey spectra were acquired using a pass-energy of 280 eV and a step size of 1 eV. The residual pressure during the measurements was always below $7*10^{-7}$ Pa. The calibration was performed using sputter- cleaned gold, silver, and copper as reference materials according to ISO15472: 2014. The accuracy was found to be 0.1 eV. High-resolution spectra were processed using CasaXPS software (v2.3.19 dev52, Casa Software Ltd., Wilmslow, Cheshire, U.K.). The background subtraction was performed applying the Shirley–Sherwood iterative method. The product of Gaussian and Lorentzian functions was used for curve fitting the experimental spectra. The electron neutralizer was utilized during the analysis, in order to compensate for sample charging. All spectra were corrected with reference to adventitious aliphatic carbon taken at 285.0 eV. Nanocrystalline anatase (TiO_2 obtained by solvothermal sol-gel)[91] and ALD (amorphous) HfO_2 were used as references. LA-ICPMS measurements were collected according to the procedure reported elsewhere.[19] The mass fraction of Ti with respect to Hf (and Zr) has been determined using a Geolas C 193 nm laser ablation system (Coherent, Göttingen, D) connected to an Element XR (Thermo Fisher, Bremen, D) sector field ICPMS. External calibration was carried out using SRM NIST 610. Internal quantum yields (iQY) were measured on a Jasco FP8500 Fluorometer, by using the methodology described in Ref.[19]. Incident light power R_{STD} was evaluated by measuring the signal, integrated in the range 250-300 nm, of a reference sample of MgO acting as diffuser. Then PL of the sample was collected in the same experimental condition and geometry. The iQY was finally calculated with the following formula

$$iQY = \frac{E}{(R_{STD} - R_{SMPL})}$$

where R_{SMPL} and E are the integrated signals over the source (250-300 nm) and emission (350-700 nm) spectral range, respectively. External quantum efficiency (EQE) was instead calculated as the ratio between emitted and incident photons ($EQE = E/R_{STD}$). All spectra were corrected for monochromator and detector response. The relative error on QY measurement has been estimated

to be 25% assuming the same consideration of Ref.[19], such as reflectivity of diffuser not exactly equal to unity, partial reflection of the window quartz placed in front of the powdered sample holder, and particle size effects.

Supporting Information

Supporting Information is available from the Wiley Online Library or from the author.

Acknowledgements

The authors are grateful to ETH Zurich for financial support. Dr. Elena Tervoort and ScopeM are kindly acknowledged for TEM analysis. Professor N. D. Spencer (ETH Zurich) is gratefully acknowledged for providing access to the XPS spectrometer while Mr. Cossu is thanked for technical assistance. The authors acknowledge the financial support of University of Cagliari and of the Fondazione Banco di Sardegna and Regione Autonoma della Sardegna Progetti Biennali di Ateneo Annualità 2016, Fondazione Sardegna CUP F72F16003070002. The EIT SPARK project (Grant No. 16290) is also acknowledged.

Received: ((will be filled in by the editorial staff))
Revised: ((will be filled in by the editorial staff))
Published online: ((will be filled in by the editorial staff))

References

[1] D. Koziej, A. Lauria, M. Niederberger, *Adv. Mater.* **2014**, *26*, 235.

[2] P. Rodríguez-Garnica, M. M. Salazar-Hernández, J. Maldonado-Estudillo, N. Saldaña-Piña, G. Sotelo-Rodríguez, B. Huichapa-Rocha, G. González-García, A. Alatorre-Ordaz, J. A. Gutiérrez, *Mater. Chem. Phys.* **2019**, *229*, 156.

[3] G. Garnweitner, M. Niederberger, *J. Mater. Chem.* **2008**, *18*, 1171.

[4] J. Y. Tsao, S. Chowdhury, M. A. Hollis, D. Jena, N. M. Johnson, K. A. Jones, R. J. Kaplar, S. Rajan, C. G. Van de Walle, E. Bellotti, C. L. Chua, R. Collazo, M. E. Coltrin, J. A. Cooper, K. R. Evans, S. Graham, T. A. Grotjohn, E. R. Heller, M. Higashiwaki, M. S. Islam,

P. W. Juodawlkis, M. A. Khan, A. D. Koehler, J. H. Leach, U. K. Mishra, R. J. Nemanich, R. C. N. Pilawa-Podgurski, J. B. Shealy, Z. Sitar, M. J. Tadjer, A. F. Witulski, M. Wraback, J. A. Simmons, *Adv. Electron. Mater.* **2018**, *4*, 1600501.

[5] M. N. Yoder, *IEEE Trans.Electron Devices* **1996**, *43*, 1633.

[6] P. Escribano, B. Julián-López, J. Planelles-Aragó, E. Cordoncillo, B. Viana, C. Sanchez, *J. Mater. Chem.* **2008**, *18*, 23.

[7] A. G. Mamalis, *J. Mater. Process. Technol.* **2007**, *181*, 52.

[8] M. Zachau, A. Konrad, *Solid State Phenom.* **2004**, *99-100*, 13.

[9] S. M. Ng, M. Koneswaran, R. Narayanaswamy, *RSC Adv.* **2016**, *6*, 21624.

[10] R. F. Gibson, *Compos.Struct.* **2010**, *92*, 2793.

[11] X. Yu, T. J. Marks, A. Facchetti, *Nat. Mater.* **2016**, *15*, 383.

[12] S. P. Suriyaraj, R. Selvakumar, *RSC Adv.* **2016**, *6*, 10565.

[13] A.-L. Bulin, M. Broekgaarden, D. Simeone, T. Hasan, *Oncotarget* **2019**, *10*, 2625.

[14] N. C. George, K. A. Denault, R. Seshadri, *Annu. Rev. Mater. Res.* **2013**, *43*, 481.

[15] R. Martínez-Martínez, E. Álvarez, A. Speghini, C. Falcony, U. Caldiño, *J. Mater. Res.* **2011**, *25*, 484.

[16] T. J. Hajagos, C. Liu, N. J. Cherepy, Q. Pei, *Adv. Mater.* **2018**, *30*, 1706956.

[17] C. Dujardin, D. Amans, A. Belsky, F. Chaput, G. Ledoux, A. Pillonnet, *IEEE Trans. Nucl. Sci.* **2010**, *57*, 1348.

[18] H.-C. Huang, S. Barua, G. Sharma, S. K. Dey, K. Rege, *J. Controlled Release* **2011**, *155*, 344.

[19] I. Villa, A. Vedda, M. Fasoli, R. Lorenzi, N. Kränzlin, F. Rechberger, G. Ilari, D. Primc, B. Hattendorf, F. J. Heiligtag, M. Niederberger, A. Lauria, *Chem. Mater.* **2016**, *28*, 3245.

[20] P. V. Pikhitsa, C. Kim, S. Chae, S. Shin, S. Jung, M. Kitaura, S.-i. Kimura, K. Fukui, M. Choi, *Appl. Phys. Lett.* **2015**, *106*, 183106.

[21] J. Ji, A. M. Colosimo, W. Anwand, L. A. Boatner, A. Wagner, P. S. Stepanov, T. T. Trinh, M. O. Liedke, R. Krause-Rehberg, T. E. Cowan, F. A. Selim, *Sci. Rep.* **2016**, *6*, 31238.

[22] K. Smits, L. Grigorjeva, D. Millers, A. Sarakovskis, J. Grabis, W. Lojkowski, *J. Lumin.* **2011**, *131*, 2058.

[23] E. G. Seebauer, K. W. Noh, *Mater. Sci. Eng. R Rep.* **2010**, *70*, 151.

[24] M. Haase, H. Schäfer, *Angew. Chem., Int. Ed.* **2011**, *50*, 5808.

[25] Y. Liu, D. Tu, H. Zhu, X. Chen, *Chem. Soc. Rev.* **2013**, *42*, 6924.

[26] A. Lauria, I. Villa, M. Fasoli, M. Niederberger, A. Vedda, *ACS Nano* **2013**, *7*, 7041.

[27] Y. Liu, W. Luo, H. Zhu, X. Chen, *J. Lumin.* **2011**, *131*, 415.

[28] J. T. Luo, X. Y. Zhu, B. Fan, F. Zeng, F. Pan, *J. Phys. D: Appl. Phys.* **2009**, *42*, 115109.

[29] S. Nakayama, M. Sakamoto, *J. Mater. Res. Technol.* **2016**, *5*, 289.

[30] C. Zhang, J. Lin, *Chem. Soc. Rev.* **2012**, *41*, 7938.

[31] B. M. Tissue, *Chem. Mater.* **1998**, *10*, 2837.

[32] C. Dujardin, E. Auffray, E. Bourret-Courchesne, P. Dorenbos, P. Lecoq, M. Nikl, A. N. Vasil'ev, A. Yoshikawa, R. Zhu, *IEEE Trans. Nucl. Sci.* **2018**, *65*, 1977.

[33] H. A. Höppe, *Angew. Chem., Int. Ed.* **2009**, *48*, 3572.

[34] S. M. Woodley, S. Hamad, J. A. Mejias, C. R. A. Catlow, *J. Mater. Chem.* **2006**, *16*, 1927.

[35] F. Cardarelli, *Materials Handbook: A Concise Desktop Reference*, 2nd ed.; Springer Verlag: New York, 2018.

[36] T. Taniguchi, N. Sakamoto, T. Watanabe, N. Matsushita, M. Yoshimura, *J. Phys. Chem. C* **2008**, *112*, 4884.

[37] N. Pinna, G. Garnweitner, M. Antonietti, M. Niederberger, *Adv. Mater.* **2004**, *16*, 2196.

[38] J. De Roo, K. De Keukeleere, J. Feys, P. Lommens, Z. Hens, I. Van Driessche, *J. Nanopart. Res.* **2013**, *15*, 1778.

[39] C.-K. Lee, E. Cho, H.-S. Lee, C. S. Hwang, S. Han, *Phys. Rev. B* **2008**, *78*, 012102.

[40] S. Kumar, S. B. Rai, C. Rath, *Phys. Chem. Chem. Phys.* **2017**, *19*, 18957.

[41] S. Lange, V. Kiisk, J. Aarik, M. Kirm, I. Sildos, *Phys. Status Solidi C* **2007**, *4*, 938.

[42] A. D. Furasova, A. F. Fakhardo, V. A. Milichko, E. Tervoort, M. Niederberger, V. V. Vinogradov, *Colloids Surf., B* **2017**, *154*, 21.

[43] C. LeLuyer, M. Villanueva-Ibañez, A. Pillonnet, C. Dujardin, *J. Phys. Chem. A* **2008**, *112*, 10152.

[44] I. Villa, C. Villa, A. Monguzzi, V. Babin, E. Tervoort, M. Nikl, M. Niederberger, Y. Torrente, A. Vedda, A. Lauria, *Nanoscale* **2018**, *10*, 7933.

[45] V. Kiisk, S. Lange, K. Utt, T. Tätte, H. Mändar, I. Sildos, *Phys. B (Amsterdam, Neth.)* **2010**, *405*, 758.

[46] M. Kirm, J. Aarik, M. Jürgens, I. Sildos, *Nucl. Instrum. Methods Phys. Res., Sect. A* **2005**, *537*, 251.

[47] I. Villa, A. Lauria, F. Moretti, M. Fasoli, C. Dujardin, M. Niederberger, A. Vedda, *Phys. Chem. Chem. Phys.* **2018**, *20*, 15907.

[48] A. Pucci, G. Clavel, M.-G. Willinger, D. Zitoun, N. Pinna, *J. Phys. Chem. C* **2009**, *113*, 12048.

[49] S. Pokhriyal, S. Biswas, *AIP Conf. Proc.* **2016**, *1728*, 020457.

[50] M. Liu, L. D. Zhang, G. He, X. J. Wang, M. Fang, *J. Appl. Phys.* **2010**, *108*, 024102.

[51] D. Muñoz Ramo, A. L. Shluger, G. Bersuker, *Phys. Rev. B* **2009**, *79*, 035306.

[52] E. Cockayne, *J. Appl. Phys.* **2008**, *103*, 084103.

[53] V. V. Atuchin, M. S. Lebedev, I. V. Korolkov, V. N. Kruchinin, E. A. Maksimovskii, S. V. Trubin, *J. Mater. Sci.: Mater. Electron.* **2019**, *30*, 812.

[54] S. Nakayama, I. Nitani, T. Asahi, M. Shiomi, T. Miyata, *J. Ceram. Soc. Jpn.* **2016**, *124*, 950.

[55] B. P. Chandra, *J. Lumin.* **2010**, *130*, 2218.

[56] D. Nakauchi, N. Kawaguchi, T. Yanagida, *Opt. Mater.* **2019**, *90*, 227.

[57] K. Fiaczyk, A. J. Wojtowicz, W. Drozdowski, K. Brylew, E. Zych, *Radiat. Meas.* **2016**, *90*, 140.

[58] K. Fiaczyk, A. J. Wojtowicz, E. Zych, *J. Phys. Chem. C* **2015**, *119*, 5026.

[59] S. S. Lucky, K. C. Soo, Y. Zhang, *Chem. Rev.* **2015**, *115*, 1990.

[60] M. Niederberger, G. Garnweitner, N. Pinna, G. Neri, *Prog. Solid State Chem.* **2005**, *33*, 59.

[61] D. Günther, B. Hattendorf, *TrAC, Trends Anal. Chem.* **2005**, *24*, 255.

[62] D. H. Triyoso, R. I. Hegde, J. K. Schaeffer, D. Roan, P. J. Tobin, S. B. Samavedam, B. E. White, R. Gregory, X. D. Wang, *Appl. Phys. Lett.* **2006**, *88*, 222901.

[63] D. H. Triyoso, R. I. Hegde, X. D. Wang, M. W. Stoker, R. Rai, M. E. Ramon, B. E. White, P. J. Tobin, *J. Electrochem. Soc.* **2006**, *153*, G834.

[64] L. Gao, L. Zhou, J. Feng, L. Bai, C. Li, Z. Liu, J.-L. Soubeyroux, Y. Lu, *Ceram. Int.* **2012**, *38*, 2305.

[65] V. Miikkulainen, M. Leskelä, M. Ritala, R. L. Puurunen, *J. Appl. Phys.* **2013**, *113*, 021301.

[66] E. Rauwel, C. Dubourdieu, B. Holländer, N. Rochat, F. Ducroquet, M. D. Rossell, G. Van Tendeloo, B. Pelissier, *Appl. Phys. Lett.* **2006**, *89*, 012902.

[67] S. Kumar, S. B. Rai, C. Rath, *Phys. Chem. Chem. Phys.* **2017**, *19*, 18957.

[68] S. Kumar, S. B. Rai, C. Rath, *J. Appl. Phys.* **2018**, *123*, 055108.

[69] I. Martínez-Merlín, A. I. Ramos-Guerra, U. Balderas, R. G. Casañas-Pimentel, C. Falcony, *Ceram. Int.* **2019**, *45*, 11362.

[70] U. Troitzsch, *J. Am. Ceram. Soc.* **2006**, *89*, 3201.

[71] A. Aronne, M. Fantauzzi, C. Imparato, D. Atzei, L. De Stefano, G. D'Errico, F. Sannino, I. Rea, D. Pirozzi, B. Elsener, P. Pernice, A. Rossi, *RSC Adv.* **2017**, *7*, 2373.

[72] H. Hernández-Arriaga, E. López-Luna, E. Martínez‐Guerra, M. M. Turrubiartes, A. G. Rodríguez, M. A. Vidal, *J. Appl. Phys.* **2017**, *121*, 064302.

[73] V. A. Gritsenko, D. R. Islamov, T. V. Perevalov, V. S. Aliev, A. P. Yelisseyev, E. E. Lomonova, V. A. Pustovarov, A. Chin, *J. Phys. Chem. C* **2016**, *120*, 19980.

[74] V. A. Pustovarov, T. P. Smirnova, M. S. Lebedev, V. A. Gritsenko, M. Kirm, *J. Lumin.* **2016**, *170*, 161.

[75] D. Muñoz Ramo, J. L. Gavartin, A. L. Shluger, G. Bersuker, *Phys. Rev. B* **2007**, *75*, 205336.

[76] M. Shang, C. Li, J. Lin, *Chem. Soc. Rev.* **2014**, *43*, 1372.

[77] E. V. Ivanova, M. V. Zamoryanskaya, V. A. Pustovarov, V. S. Aliev, V. A. Gritsenko, A. P. Yelisseyev, *J. Exp. Theor. Phys.* **2015**, *120*, 710.

[78] D. R. Islamov, V. A. Gritsenko, V. N. Kruchinin, E. V. Ivanova, M. V. Zamoryanskaya, M. S. Lebedev, *Phys. Solid State* **2018**, *60*, 2050.

[79] G. M. Kumar, P. Ilanchezhiyan, F. Xiao, C. Siva, A. M. Kumar, V. Yalishev, S. U. Yuldashev, T. W. Kang, *RSC Adv.* **2016**, *6*, 57941.

[80] E. Aleksanyan, M. Kirm, E. Feldbach, V. Harutyunyan, *Radiat. Meas.* **2016**, *90*, 84.

[81] S.-H. Chuang, H.-C. Lin, C.-H. Chen, *J. Alloys Compd.* **2012**, *534*, 42.

[82] E. Rauwel, A. Galeckas, P. Rauwel, *Mater. Res. Express* **2014**, *1*, 015035.

[83] J. Strand, S. K. Chulkov, M. B. Watkins, A. L. Shluger, *J. Chem. Phys.* **2019**, *150*, 044702.

[84] J. Aarik, H. Mändar, M. Kirm, L. Pung, *Thin Solid Films* **2004**, *466*, 41.

[85] G. A. M. Dalhoeven, G. Blasse, *J. Solid State Chem.* **1981**, *39*, 35.

[86] W. J. Schipper, J. J. Piet, H. J. De Jager, G. Blasse, *Mater. Res. Bull.* **1994**, *29*, 23.

[87] F. Moretti, G. Patton, A. Belsky, M. Fasoli, A. Vedda, M. Trevisani, M. Bettinelli, C. Dujardin, *J. Phys. Chem. C* **2014**, *118*, 9670.

[88] E. Dell'Orto, M. Fasoli, G. Ren, A. Vedda, *J. Phys. Chem. C* **2013**, *117*, 20201.

[89] M. Fasoli, N. Chiodini, A. Lauria, F. Moretti, A. Vedda, *Phys. Status Solidi C* **2007**, *4*, 1056.

[90] T. Yanagida, *Proc. Jpn. Acad., Ser. B* **2018**, *94*, 75.

[91] C. Frantz, A. Lauria, C. V. Manzano, C. Guerra-Nuñez, M. Niederberger, C. Storrer, J. Michler, L. Philippe, *Langmuir* **2017**, *33*, 12404.

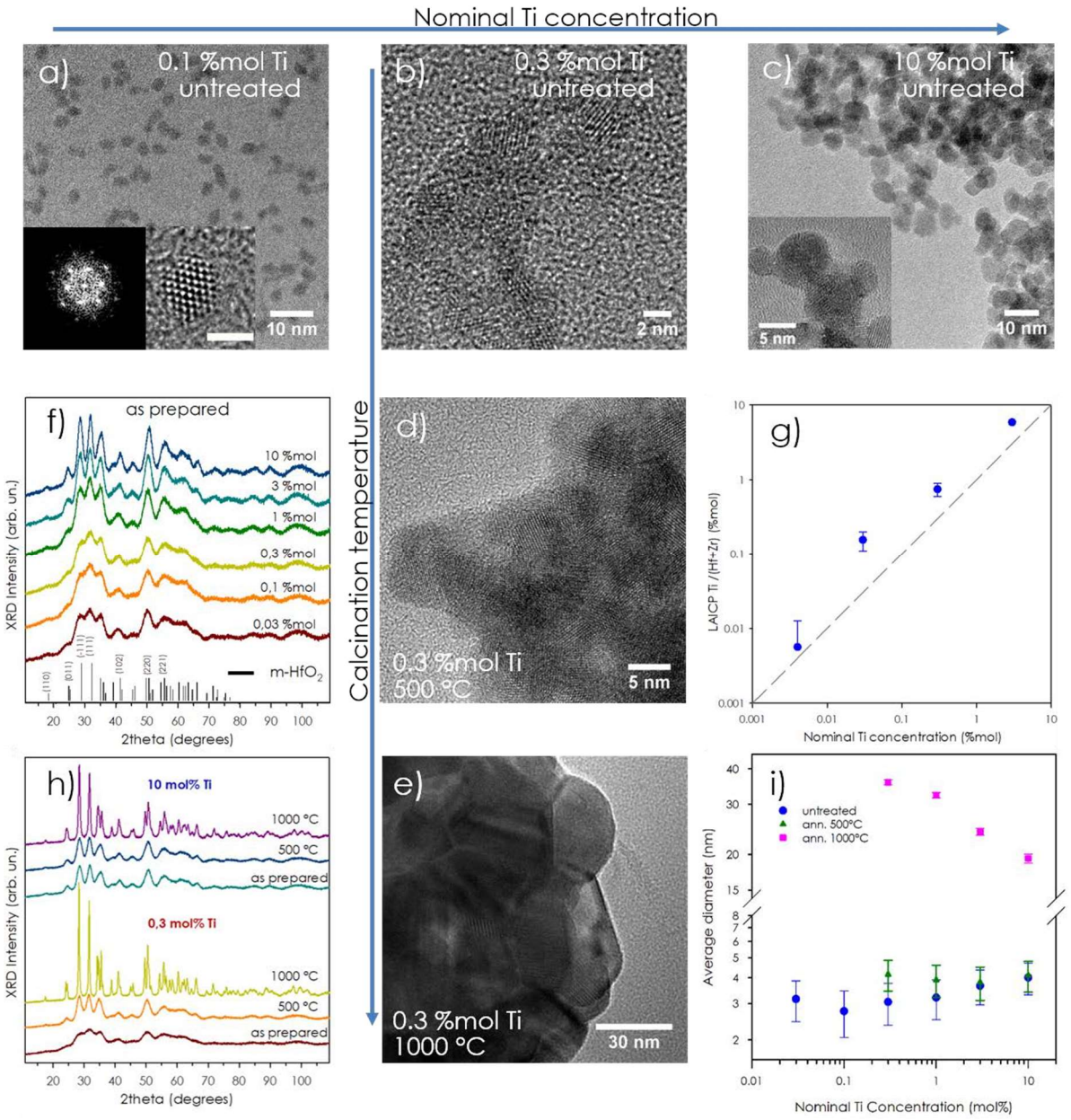

Figure 1. *Structure and morphology of Ti-doped HfO_2 NCs depending on Ti concentration and calcination temperature. a,b,c): TEM of HfO_2 nanocrystals doped by 0.1, 0.3, and 10 mol% Ti, respectively. (Insets: HR-TEM of single crystalline particles and corresponding FFT analysis). d,e): TEM images of 0.3 mol% Ti:HfO_2, calcined at 500 and 1000 °C, respectively. f): XRD patterns of as synthesized nanopowders depending on Ti doping. g): residual Ti, measured by LA-ICPMS, as a function of nominal concentration (grey dashed line: theoretical doping). h): XRD dependence on the calcination temperature for 0.3 and 10 mol% Ti-doped hafnia NPs. i): dependence on the nominal Ti concentration of the average crystal diameter (obtained by the Scherrer analysis of XRD pattern) measured on untreated (blue circles) NPs, and after calcination at 500 and 1000 °C (green triangles and pink squares, respectively).*

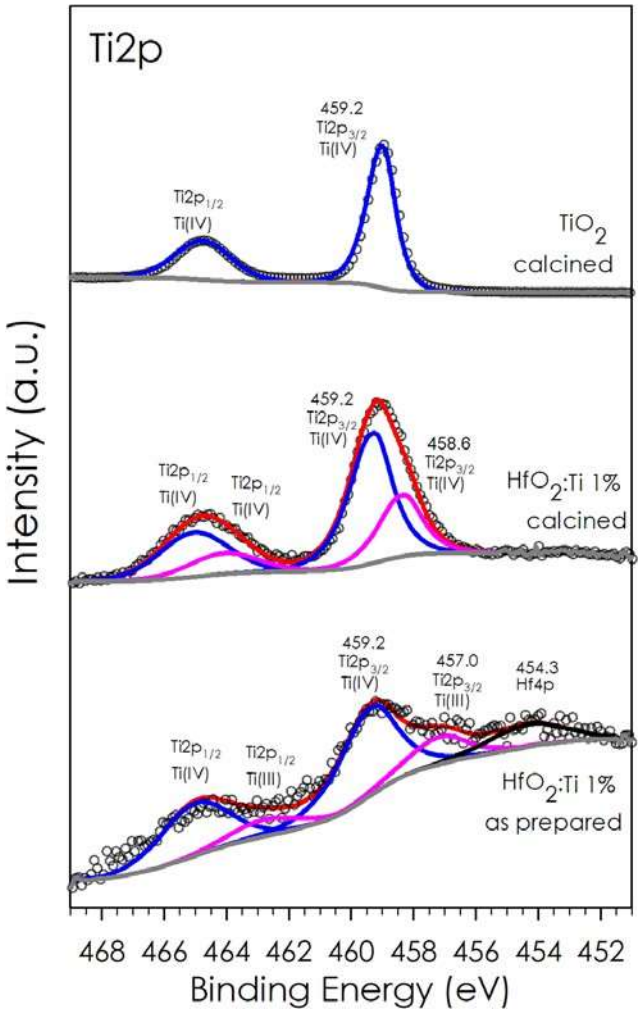

Figure 2. *XPS spectra of 1 mol% Ti:HfO_2 before and after calcination. The spectrum of calcined TiO_2 nanocrystals was recorded as a reference for Ti(IV).*

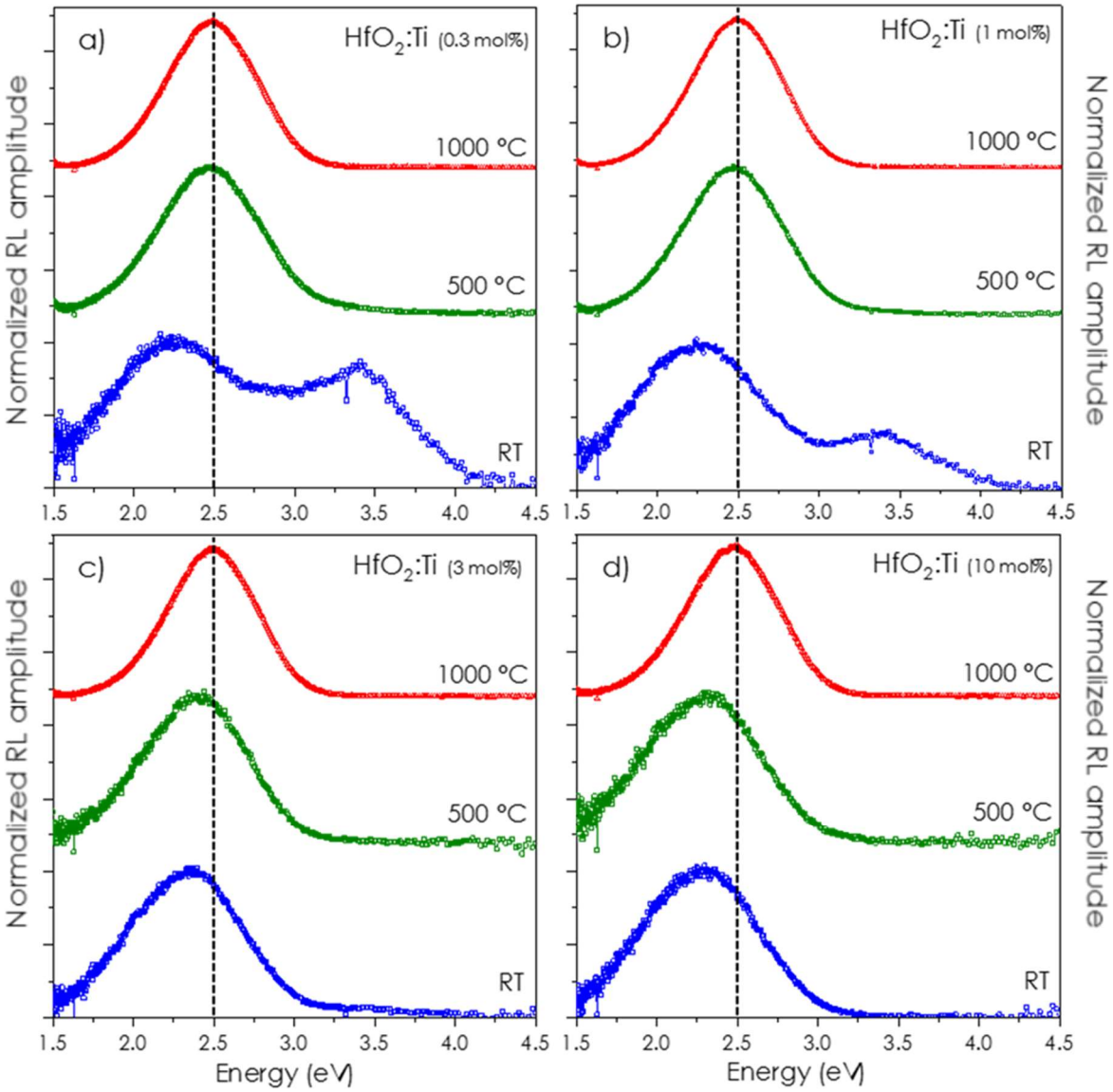

Figure 3. *Normalized RL spectra, measured at room temperature, of HfO_2:Ti nano-powders untreated (RT-blue dots), calcined at 500 °C (green squares), and at 1000°C (red triangles). Increasing Ti concentrations are here considered: a) 0.3 mol%, b) 1 mol%, c) 3 mol%, and d) 10 mol%. All spectra are corrected for the instrumental response*

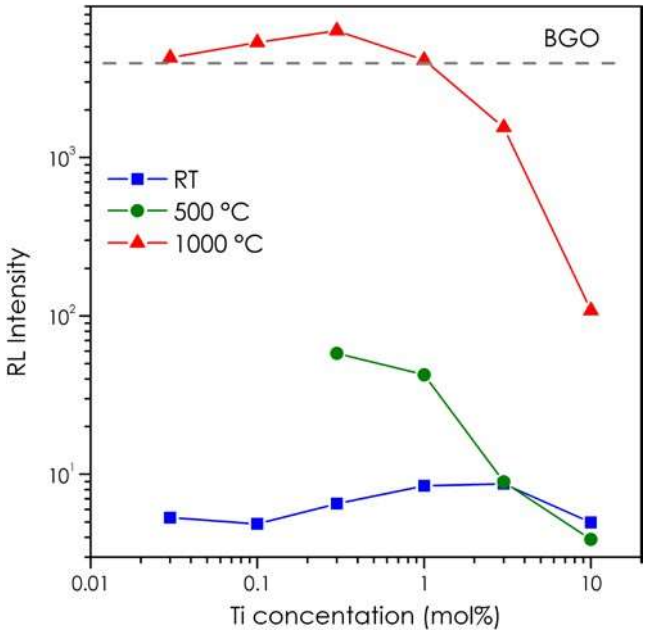

Figure 4. *Dependence of the RL intensity on Ti concentration and at different calcination temperature.*

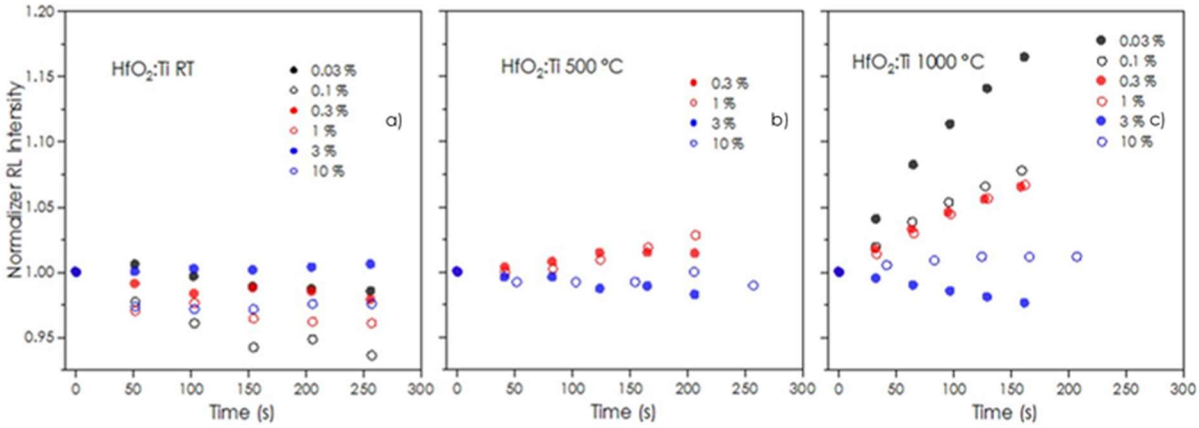

Figure 5. *Time course measurements for HfO_2:Ti nano-powders doped with different concentrations of Ti. a): as prepared powders. b): powders treated at 500 °C. c): powders treated at 1000 °C. The plots display the emission integrals depending on irradiation time.*

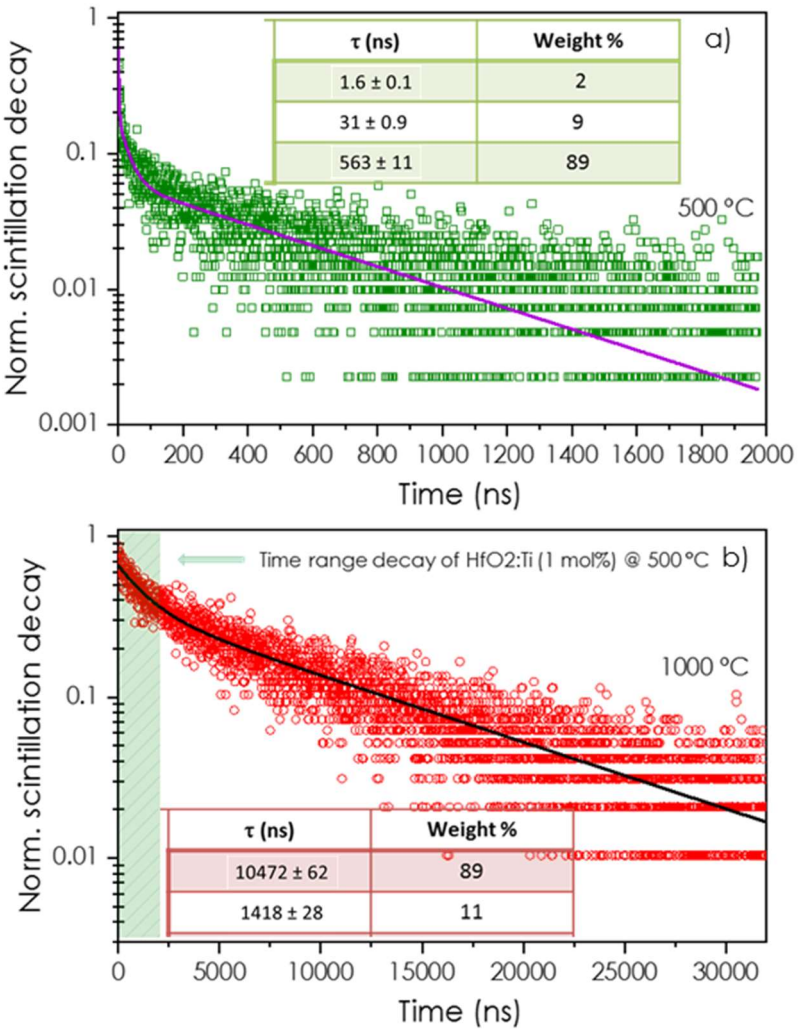

Figure 6. *Pulsed X-ray decays obtained on HfO_2:Ti treated at 500 and 1000 °C, full black dots and red circles, respectively. Full lines are fit to the experimental data. The emission wavelength has been selected by using a FL400 long pass edge filter. The green area in panel*

b) represents the time window recorded for the measurements in panel a).

WILEY-VCH

Bright visible luminescence in HfO_2 nanocrystals is activated by the incorporation of Ti(IV), with high PL quantum yield (>30%) under UV excitation. Under X-ray illumination, the high RL efficiency and a scintillation lifetime in the μs range make Ti:HfO_2 a promising material for rare-earth free nanoscintillators for X-ray detectors and medical therapy.

Keyword HfO_2 scintillator nanocrystals activated by Ti doping.

*Irene Villa, Federico Moretti, Mauro Fasoli, Antonella Rossi, Bodo Hattendorf, Christophe Dujardin, Markus Niederberger, Anna Vedda, and Alessandro Lauria**

The bright X-ray stimulated luminescence of HfO_2 nanocrystals activated by Ti ions.

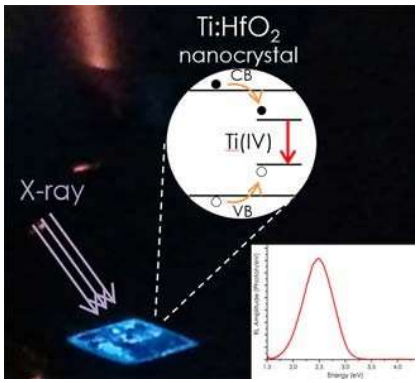

WILEY-VCH

Supporting Information

The bright X-ray stimulated luminescence of HfO_2 nanocrystals activated by Ti ions.

*Irene Villa, Federico Moretti, Mauro Fasoli, Antonella Rossi, Bodo Hattendorf, Christophe Dujardin, Markus Niederberger, Anna Vedda, and Alessandro Lauria**

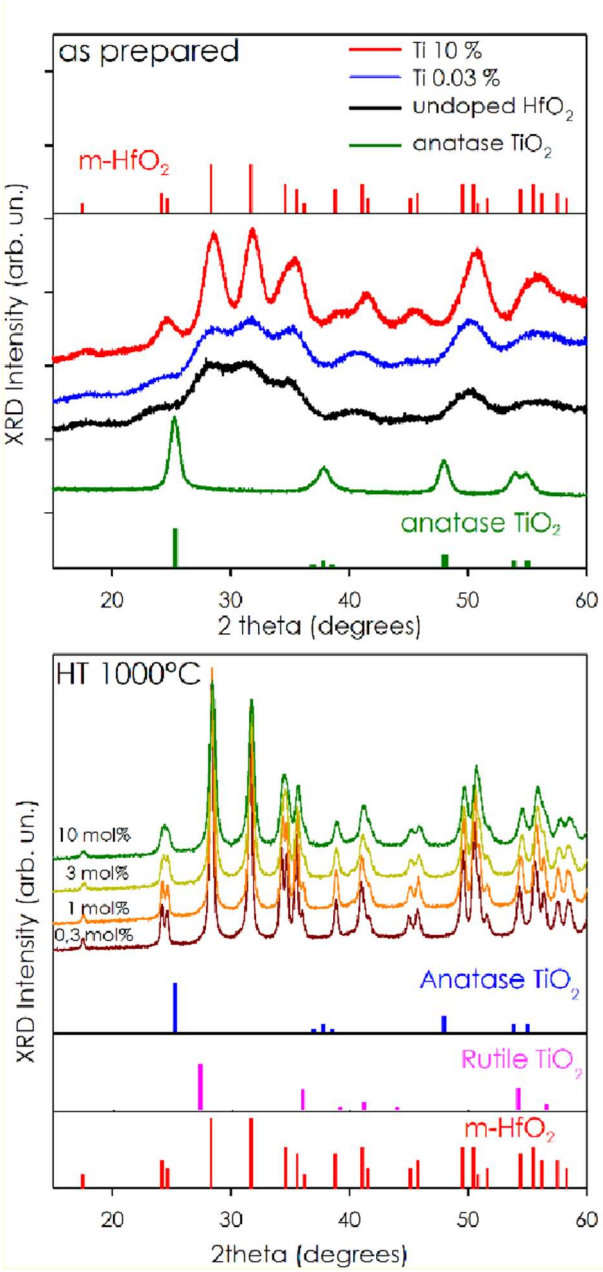

Figure S1 – Top panel: XRD of as prepared HfO_2 (black line), $Hf_{0.9997}Ti_{0.0003}O_2$ (blue line), $Hf_{0.9}Ti_{0.1}O_2$ (red line) and pure TiO_2 anatase (green line) nanocrystals. The reference patterns for anatase (PDF 00-21-1272) and monoclinic hafnia (PDF 00-006-0318) are also shown (green and red bars, respectively). Bottom panel: XRD of hafnia nanopowders doped by 0.3, 1, 3, and 10 mol% Ti, after calcination at 1000 °C. The reference patterns of titania anatase (PDF 00-21-1272),

rutile (PDF 04-008-8141), and monoclinic hafnia (PDF 00-006-0318) are also reported (blue, pink, and red bars, respectively).

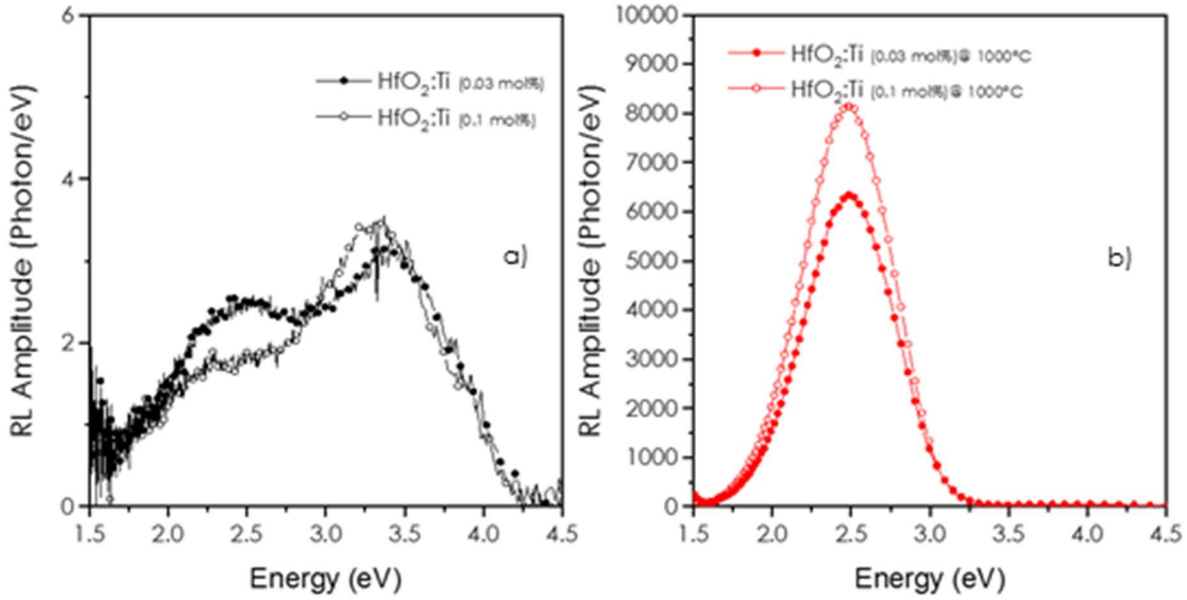

Figure S2 - RL spectra measured at room temperature of HfO_2:Ti nano-powders . In panel a) RL spectra of hafnia doped at 0.03 mol% and 0.1 mol% are displayed. Panel b) displays the RL of the same nanopowders after calcination at 1000°C. All spectra are corrected by instrumental response.

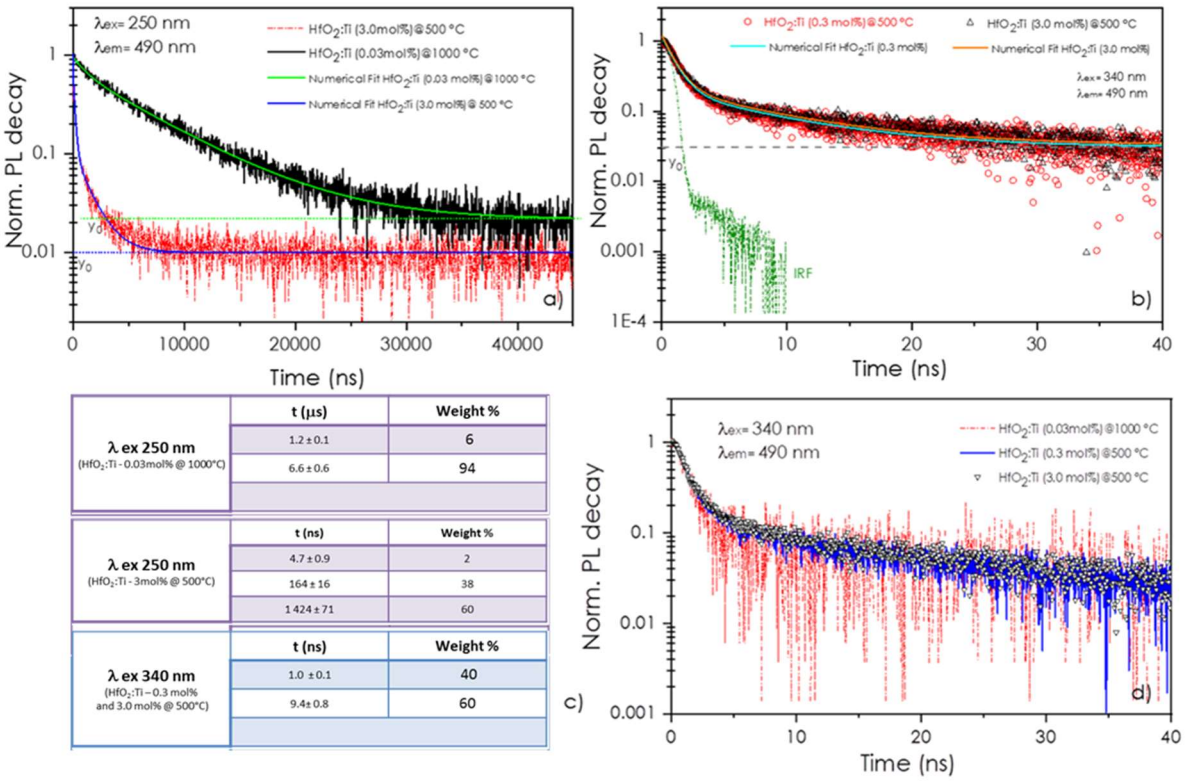

	t (µs)	Weight %
λ ex 250 nm (HfO_2:Ti - 0.03mol% @ 1000°C)	1.2 ± 0.1	6
	6.6 ± 0.6	94

	t (ns)	Weight %
λ ex 250 nm (HfO_2:Ti - 3mol% @ 500°C)	4.7 ± 0.9	2
	164 ± 16	38
	1 424 ± 71	60

	t (ns)	Weight %
λ ex 340 nm (HfO_2:Ti – 0.3 mol% and 3.0 mol% @ 500°C)	1.0 ± 0.1	40
	9.4 ± 0.8	60

Figure S3 – Decay curves of HfO_2 calcined at different temperatures and at different Ti doping concentrations. The emission, collected at 490 nm, has been stimulated by 250 nm (a) and 340 nm (b and d) pulsed excitation. Numerical

fit of the decays in a) and b) are presented together with the instrumental response in the time range of 50 ns (b); y_0 is a constant parameter added in the multi-exponential fit. The parameters of numerical fits used to model the PL decay are reported in Table (c).

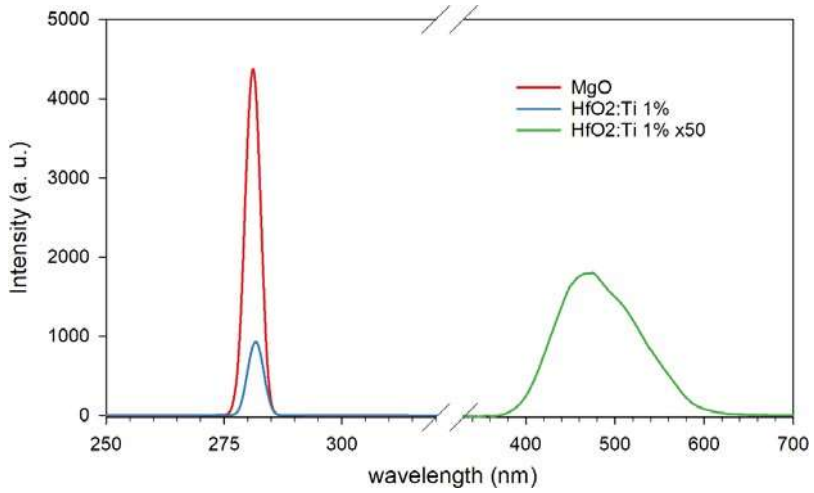

Figure S4 - PL spectra recorded on MgO and 1 mol% HfO_2:Ti calcined powders for the determination of the quantum efficiency under excitation at 280 nm.

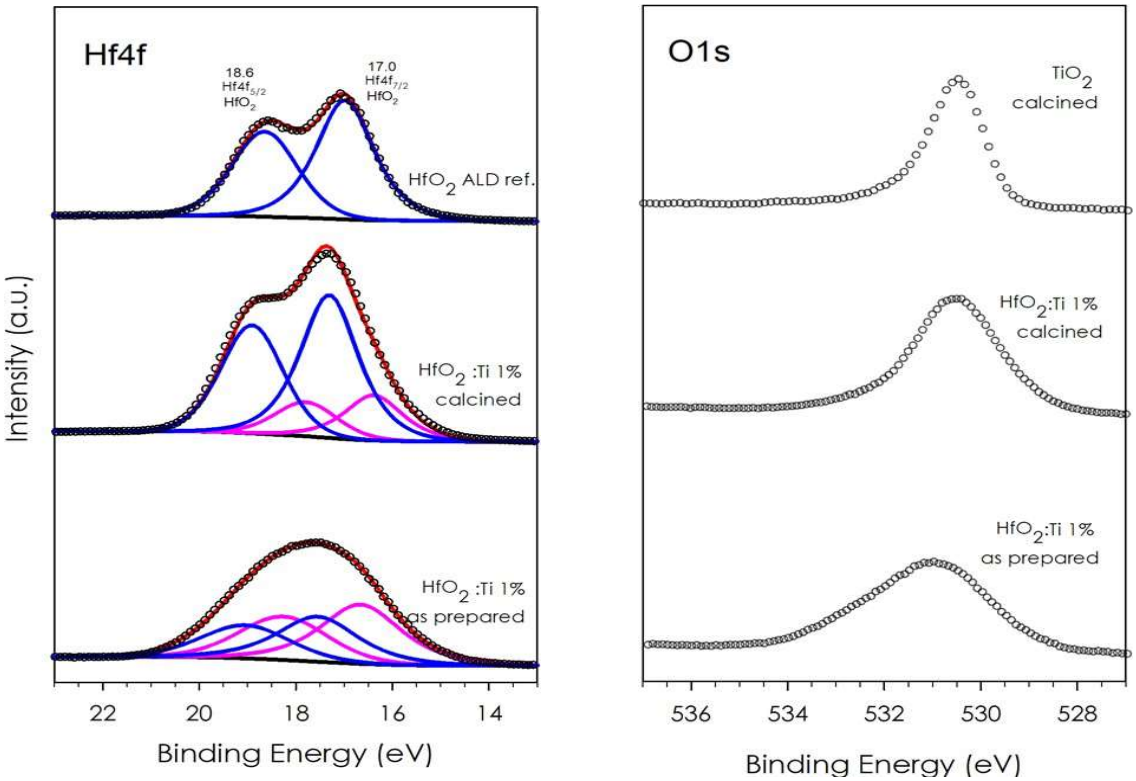

Figure S5 - Hf4f and O1s XPS spectra recorded on HfO_2:Ti 1 mol% nanopowders. The signal of TiO_2 calcined nanopowders are also shown and used as a reference for oxygen, while pure HfO_2 obtained by ALD is used as reference for the signal of Hf4f in HfO_2.

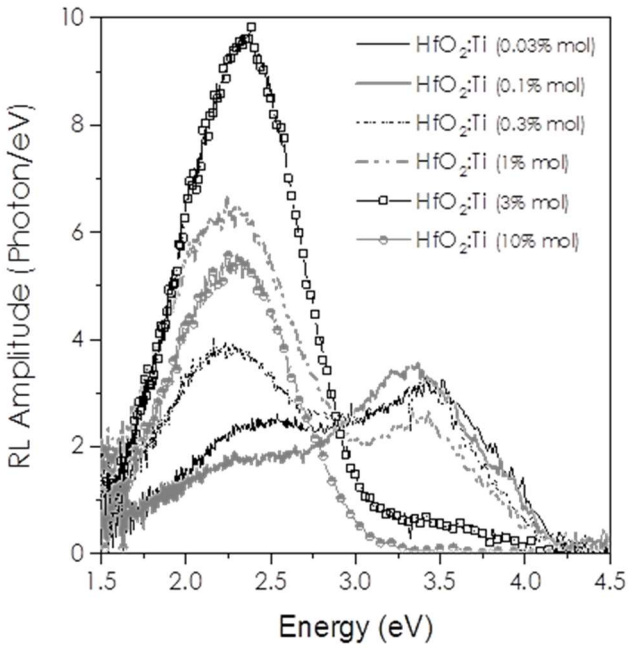

Figure S6 – RL spectra recorded at RT on as prepared HfO2:Ti nanopowders. The complex RL profile, resulting from several bands related to intrinsic defects, shows a progressive increase of the visible components with increasing Ti, whereas the UV component at around 3.4 eV diminishes with Ti concentration.